RSC Advances

PAPER

View Article Online
View Journal | View Issue

Cite this: *RSC Adv.*, 2021, **11**, 11702

Enhanced charge separation in TiO_2/nanocarbon hybrid photocatalysts through coupling with short carbon nanotubes†

Ahmed Al Mayyahi,[a] Brian M. Everhart,[a] Tej B. Shrestha,[b] Tyson C. Back[c] and Placidus B. Amama *[a]

Received 4th January 2021
Accepted 10th March 2021

DOI: 10.1039/d1ra00045d

rsc.li/rsc-advances

The interfacial contact between TiO_2 and graphitic carbon in a hybrid composite plays a critical role in electron transfer behavior, and in turn, its photocatalytic efficiency. Herein, we report a new approach for improving the interfacial contact and delaying charge carrier recombination in the hybrid by wrapping short single-wall carbon nanotubes (SWCNTs) on TiO_2 particles (100 nm) *via* a hydration-condensation technique. Short SWCNTs with an average length of 125 ± 90 nm were obtained from an ultrasonication-assisted cutting process of pristine SWCNTs (1–3 μm in length). In comparison to conventional TiO_2–SWCNT composites synthesized from long SWCNTs (1.2 ± 0.7 μm), TiO_2 wrapped with short SWCNTs showed longer lifetimes of photogenerated electrons and holes, as well as a superior photocatalytic activity in the gas-phase degradation of acetaldehyde. In addition, upon comparison with a TiO_2–nanographene "quasi-core–shell" structure, TiO_2-short SWCNT structures offer better electron-capturing efficiency and slightly higher photocatalytic performance, revealing the impact of the dimensions of graphitic structures on the interfacial transfer of electrons and light penetration to TiO_2. The engineering of the TiO_2–SWCNT structure is expected to benefit photocatalytic degradation of other volatile organic compounds, and provide alternative pathways to further improve the efficiency of other carbon-based photocatalysts.

1. Introduction

Rapid recombination of photogenerated electron–hole pairs is one of the major limitations of utilizing TiO_2 photocatalysts in applications such as water treatment,[1–3] air purification[4–9] bacterial and viral inactivation,[10,11] and self-cleaning glasses.[12–14] Most of the photogenerated electron–hole pairs recombine within 10 picoseconds (ps), which is very short compared to the 100 ps typically required for redox reactions. As a result, only a small portion (~10 percent) of the photogenerated charges, as revealed by time-resolved absorption spectroscopic studies, remain alive and able to participate in pollutant decomposition, resulting in limited photocatalytic activity.[15,16] A number of studies have shown that inhibition of charge recombination and remarkable enhancement in photocatalytic efficiency of TiO_2 can be achieved by coupling with carbon nanomaterials such as carbon nanotubes (CNTs), graphene, and fullerene.[17–21] The coupling leads to formation of a Schottky barrier, through which electrons efficiently travel from TiO_2 with a higher Fermi level to the carbon nanomaterial with a lower Fermi level until equilibrium is attained.[22,23] In addition, the high electron-storage capacity of the graphitic structure (one electron per 32 carbon atoms) can serve as electron reservoirs or sinks, decreasing the recombination probability of the photogenerated charges in the hybrid material and enhancing photocatalytic activity.[22]

The improved charge separation in TiO_2–nanocarbon hybrid structures depends largely on the quality of interfacial contact between TiO_2 and the graphitic structure, and the structural and surface properties of the hybrid components.[21,24–30] A knowledge gap that still exists is how the graphitic structures and their geometries affect the coupling and interfacial contacts of the components in the hybrid. The rate of electron transport and subsequent separation of photogenerated charges in conventional TiO_2–nanocarbon composites are still hampered by nonuniform coating or poor dispersion induced by TiO_2 aggregation on graphene sheets or CNT walls. Therefore, in light of the great promise shown by TiO_2–nanocarbon hybrids in photocatalysis, research efforts have focused on tailoring the heterojunctions and schottky barriers to achieve efficient shuttling of electrons and promote electron–hole separation, as well as induce visible light excitation. It is well-established in the literature that charge recombination is inhibited on

[a]Tim Taylor Department of Chemical Engineering, Kansas State University, Manhattan, KS 66506, USA. E-mail: pamama@ksu.edu
[b]Nanotechnology Innovation Center of Kansas State, Manhattan, KS 66506, USA
[c]Materials and Manufacturing Directorate, Air Force Research Laboratory, Wright-Patterson AFB, OH 45433, USA

† Electronic supplementary information (ESI) available. See DOI: 10.1039/d1ra00045d

a variety of TiO_2–CNT hybrids consisting of a thin, uniform TiO_2 layer on individual multi-walled CNTs (MWCNTs) or TiO_2 aggregates supported on CNTs.[29,31–34] However, the trade-off relation between electron–hole concentration and separation efficiency in conventional TiO_2-coated CNT composites remains a significant impediment to maximizing the photocatalytic activity.[28] To this end, TiO_2 wrapped with graphene has been considered as an alternative to the TiO_2/CNT core–shell (or TiO_2-coated CNT) structure, as the concentration of photogenerated charges can be optimized without sacrificing separation efficiency.[19,35]

Significant differences exist in hybrid structures formed with either CNTs or graphene. Graphene, a two-dimensional (2D) structure with several nanometers of width and high stacking tendency, can generate a "shell-like" structure consisting of several graphene layers on TiO_2, preventing light penetration.[36,37] Another complication associated with graphene is the unavoidable electron scattering that may reduce the electron transport rate and promote charge recombination.[37] On the other hand, harnessing the one-dimensional (1D) single-wall CNT (SWCNT) structures in TiO_2 hybrids not only provides well-defined routes for electron transport, but also their small size compared to MWCNTs and graphene sheets provide a degree of freedom for optimizing charge separation without compromising light absorption.[38–42] A consensus from the aforementioned studies is that the structure of nanocarbons (*i.e.*, the size of graphene or length of CNTs) is a crucial factor in controlling the quality of interfacial contact and subsequent charge separation. In particular, Kim *et al.*[36] revealed a superior photocatalytic activity for TiO_2 hybrids formed with nano-sized graphene (or nanographene) sheets in comparison to those formed with micro-sized graphene; the wrapping of nanographene on TiO_2 particles in the former hybrid maximized the interfacial contact between the components, resulting in superior charge separation and photocatalytic activity. Similarly, we hypothesize that cutting long SWCNTs into high populations of open-ended tubes with high degrees of functionalization and density of active sites, as well as short lengths that can effectively wrap a large TiO_2 particle (~100 nm), can lead to enhanced interactions with TiO_2 particles that will promote the photocatalytic process. Although many studies have investigated the influence of coupling SWCNTs with TiO_2, all reported works employed SWCNTs with lengths in the micrometer range.

In this study, we report for the first time the wrapping of large TiO_2 particles (~100 nm) with short SWCNTs (125 ± 90 nm in length) obtained from an ultrasonication-assisted cutting process. The resulting TiO_2–SWCNT hybrid photocatalyst exhibits enhanced interfacial contact and charge separation. The short, highly functionalized and dispersed SWCNTs, in the presence of TiO_2, initiated formation of Ti–O–C bonds *via* intermolecular interactions, resulting in TiO_2 nanoparticles or nanoparticle aggregates that are partially wrapped by SWCNTs. In comparison to conventional TiO_2–SWCNT composites synthesized using long SWCNTs (1.2 ± 0.7 μm), TiO_2 wrapped with short SWCNTs showed longer lifetimes of photogenerated electrons and holes, as well as a superior photocatalytic activity in the gas-phase degradation of acetaldehyde. In addition, upon comparison with a TiO_2–nanographene "quasi-core–shell" structure, the novel TiO_2–SWCNT composite offers superior electron-capturing efficiency and slightly higher photocatalytic performance, revealing the impact of the dimension of graphitic structures on the interfacial transfer of electrons and light penetration to TiO_2.

2. Experimental section

2.1. Synthesis of TiO_2–SWCNT composites

Purified SWCNTs (1–2 nm in diameter and 1–3 μm in length) were functionalized by refluxing with HNO_3 (70%) at 150 °C for two hours. A known amount of functionalized SWCNTs were dispersed in ethanol and sonicated at 25 °C for four hours to produce the short SWCNTs. After the sonication-assisted cutting process, the resulting suspension was allowed to settle for 15 minutes and the supernatant was slowly added to the TiO_2–ethanol dispersion (50 mg in 50 mL ethanol) under sonication, followed by robust stirring overnight at pH = 3.4. The sonicator (Branson, CPX5800H) operated at 100 W and 40 kHz. The TiO_2 particles (anatase, 99.9%, 100 nm) were purchased from US Research Nanomaterials, Inc. The TiO_2–SWCNT hybrid synthesized from short SWCNTs (hereafter referred to as TiO_2-short SWCNT) was collected by filtration using a membrane with average pore size of 0.2 μm and dried at 60 °C. For TiO_2–SWCNT hybrids synthesized from long SWCNTs, the same procedure was followed without subjecting the long SWCNTs to ultrasonication-assisted cutting; the resulting hybrid is hereafter referred to as TiO_2-long SWCNT. Unless stated otherwise, the amount of SWCNTs used in the standard sample is 1 wt%.

2.2. Synthesis of TiO_2–nanographene composites

The graphite powder was oxidized by the modified Hummer method.[43–45] The graphene oxide (GO) produced was treated with a mixture of HCl and $KMnO_4$ to produce the nanographene oxide. GO (0.05 g) was dispersed in 50 mL of concentrated HCl, and then 0.05 g of $KMnO_4$ was slowly added under robust stirring. After one hour of stirring at 40 °C, the resulting slurry was cooled in an ice bath. Then, H_2O_2 solution (5 mL H_2O_2 and 95 mL distilled water) was slowly added with continued stirring for one hour, followed by sonication for 30 minutes to exfoliate the nanographene oxide. The final product was collected by filtration using similar conditions in Section 2.1 and oven-dried at 60 °C.

The TiO_2–nanographene composite (0.7 wt% nanographene) was synthesized by dispersing a known amount of nanographene oxide in ethanol by sonication, and the resulting slurry was slowly added to the TiO_2–ethanol dispersion (50 mg in 50 mL distilled water) under stirring at pH = 3.5, followed by robust stirring overnight. The brownish powder obtained was transferred to a Teflon-lined, hydrothermal synthesis autoclave reactor and heated at 120 °C for 24 hours to reduce the nanographene oxide. The final product (hereafter referred to as TiO_2–nanographene) was washed repeatedly with 1 M HCl and distilled water, collected by filtration and dried at 60 °C.

2.3. Characterization methods

X-ray diffraction (XRD) patterns were collected on a Rigaku Miniex II X-ray diffractometer with Cu Kα radiation ($\lambda = 1.5418$ Å) at 40 kV and 40 mA. The Raman spectra were acquired *via* an iHR550 spectrometer with a laser excitation wavelength of 532 nm. Catalyst morphology was characterized by a field-emission scanning electron microscope (SEM, Hitachi S5200) equipped with energy-dispersive X-ray spectroscopy (EDS), and a transmission electron microscope (TEM, FEI Talos) operating at 200 kV. For TEM analysis, a small amount of the sample was dispersed in ethanol by sonication and dropped onto a copper microgrid coated with lacy carbon film. X-ray photoelectron spectroscopic (XPS) measurements were collected *via* a Kratos Ultra XPS system at 1.0×10^{-9} Torr. A monochromatic Al Kα source ($h\nu = 1486.6$ eV) operating at 10 mA and 12 keV (120 W) was used to collect the spectra. The effect of charging was reduced by a charge neutralizer. Survey spectra were collected at 160 eV pass energy with 1 eV step and 100 ms contact time. For the high-resolution scans, spectra were collected at 20 eV pass energy with 0.1 eV step and 100 ms contact time. The photoluminescence (PL) spectra were acquired *via* a spectraMax i3x multi-mode microplate reader over the range of 400–700 nm using an excitation wavelength of 360 nm.

2.4. Evaluation of photocatalytic activity

The photocatalytic activity was tested by measuring the change in concentration of gas phase acetaldehyde as a function of irradiation time. The photocatalyst (100 mg) was placed in a 750 mL borosilicate batch reactor surrounded by light sources (two 25 W Sylvania 21703 (356 nm) bulbs and two 13 W Repti-Sun 10.0 UV/B bulbs (280–320 nm) with intensity of 6.5 W m^{-2}). One thousand ppmv of acetaldehyde gas was injected into the reactor *via* a syringe. After equilibrium between gaseous and adsorbed phases was attained, UV irradiation was started and the decrease in concentration was measured *via* an SRI 310C gas chromatograph equipped with a Restek silica gel column (8046-895, 6 ft length, 2 mm ID), on-column injection, and flame ionization detector (FID). According to the experimental data, acetaldehyde degradation by TiO_2-short SWCNT, TiO_2-long SWCNT and TiO_2–nanographene fitted to a pseudo first-order reaction represented by eqn (1):

$$\frac{c}{c_0} = e^{-kt} \quad (1)$$

where k is the apparent constant of reaction rate, c is the concentration of acetaldehyde and t is the reaction time.

3. Results

3.1. Morphology, structure, composition, and interfacial properties

The SEM image in Fig. 1a reveals TiO_2 particles are partially wrapped by short SWCNTs (TiO_2-short SWCNT), a phenomenon that occurs uniformly over a large area on TiO_2 particles. EDS mapping of TiO_2-short SWCNT (Fig. 1b) reveals the co-existence

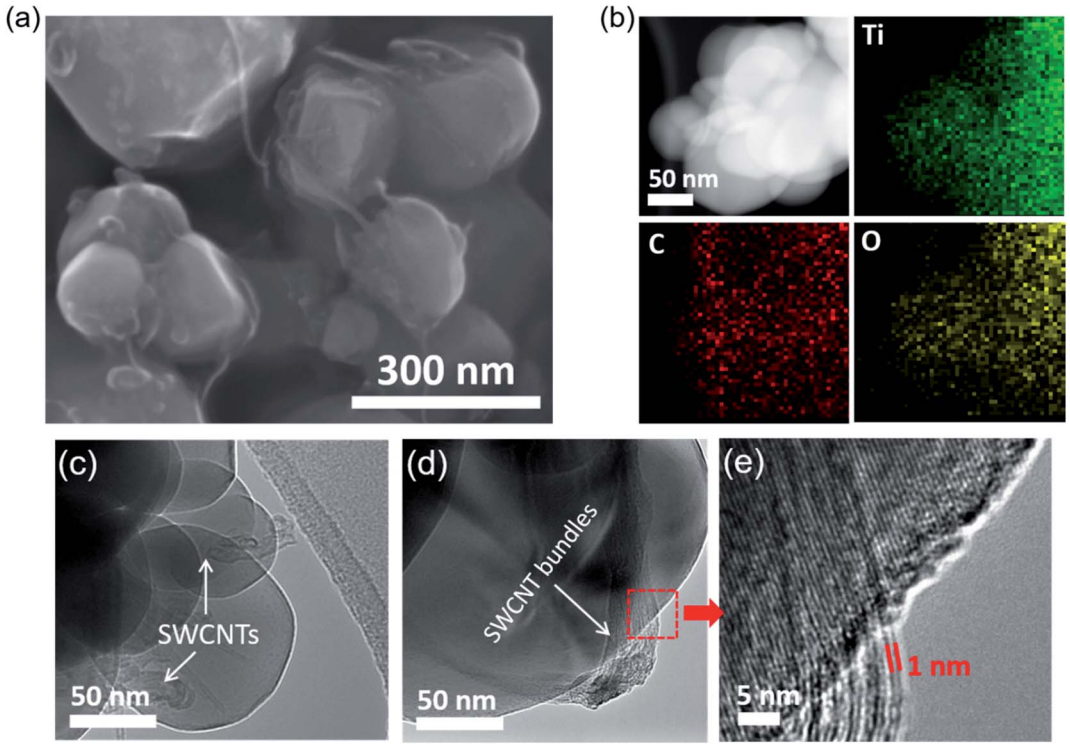

Fig. 1 (a) SEM image of TiO_2-short SWCNT; (b) EDS mapping of TiO_2-short SWCNT; (c) and (d) TEM images of (a) showing TiO_2 particles decorated with short SWCNTs and SWCNT bundles with arrows showing interactions between a TiO_2 particle and individual SWCNTs or bundles. (e) A zoom-in high-resolution TEM image of the region in (d) with a red square.

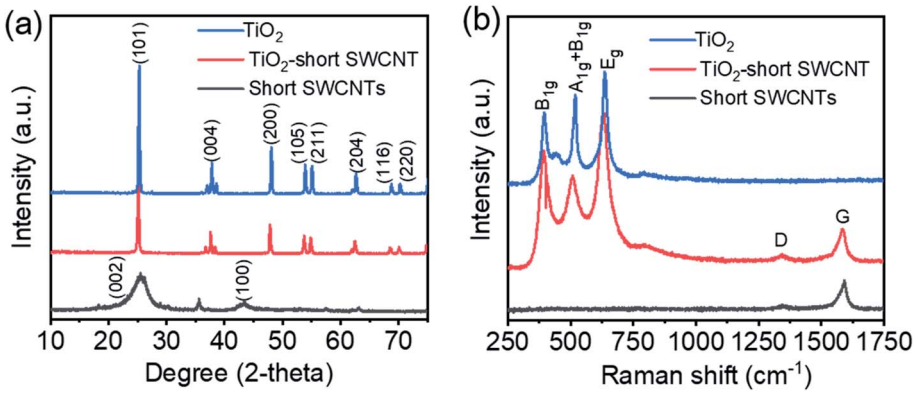

Fig. 2 (a) XRD profiles of TiO_2, TiO_2-short SWCNT, and short SWCNTs. (b) Raman spectra of TiO_2, TiO_2-short SWCNT, and short SWCNTs.

of carbon, titanium, and oxygen, with atomic concentrations of 15.75%, 34.23%, and 32.62%, respectively. The partial wrapping of TiO_2 particles by individual SWCNTs or SWCNT bundles is further confirmed by the TEM images in Fig. 1c and d while the low-magnification SEM image in Fig. S1† demonstrates the wrapping phenomenon occurs across a large area of the sample. The TEM images (Fig. 1c and d) show short SWCNTs of different lengths either as bundles or isolated nanotubes on a TiO_2 particle. From SEM and TEM data, it is apparent intimate interactions between the SWCNTs and TiO_2 exist. The high-resolution TEM images in Fig. S2† show the SWCNTs form a network on TiO_2 particles. The small diameters of SWCNTs (~1.5 nm) compared to that of TiO_2 particles (~100 nm) implies a large fraction of the incident light can participate in excitation of TiO_2. In other words, the deposition of the short SWCNTs does not appear to lead to significant light scattering or prevent light absorption by TiO_2. However, aggregation of the short SWCNTs was observed in photocatalyst samples with higher SWCNT concentrations as shown in the TiO_2-short SWCNT sample with 3 wt% SWCNTs (Fig. S3†).

XRD patterns of short SWCNTs, TiO_2, and TiO_2-short SWCNT are shown in Fig. 2a. The peaks at $2\theta = 55.1°$, 54.0°, 48.1°, 37.9°, and 25.4° are respectively indexed to (211), (105), (200), (004), and (101) facets, typical for anatase TiO_2. The sharp and intense peaks affirm the high crystallinity of the photocatalysts, whereas the absence of peaks associated with impurities is evidence of their high quality. The peaks at 26.8° and 42.8°, usually attributed to (002) and (100) crystal planes of SWCNTs, were not detected in TiO_2-short SWCNT, due to the low SWCNT concentration (1 wt%). However, the addition of SWCNTs slightly reduced the relative intensity of TiO_2 peaks, an observation consistent with other studies.[46,47] Raman spectra (Fig. 2b) show the characteristic peaks of anatase TiO_2 at 397, 515, and 639 cm^{-1}.[48] The characteristic anatase peaks (B_{1g}, A_{1g} + B_{1g}, and E_g) were observed in TiO_2-short SWCNT, accompanied by the disordered carbon-induced D-band at 1350 cm^{-1}, and the G-band at 1583 cm^{-1} that represents sp^2 carbon from SWCNTs. The slight shift in anatase modes observed in the Raman and XRD spectra generally correlates with the external perturbation by SWCNTs and the corresponding substitution of Ti^{4+} by C atoms, resulting in the formation of Ti–O–C bonds in the TiO_2 lattice.[49–52] However, band gaps of TiO_2 and TiO_2-short SWCNT (calculated from UV-Vis spectra in Fig. S4†) are 3.22 and 3.19 eV, respectively, suggesting low-carbon doping in the composite.

An XPS survey spectrum of TiO_2-short SWCNT confirms the presence of Ti, O, and C (Fig. 3a). The high-resolution XPS spectrum of Ti 2p (Fig. 3b) shows two peaks located at 459.5 and 465.2 eV attributed to Ti $2p_{3/2}$ and Ti $2p_{1/2}$, respectively, which are typical binding energies of the Ti^{4+} valance state.[53] The O 1s spectrum, shown in Fig. 3c, is fitted with three peak components. The component at 530.7 eV corresponds to Ti–O–Ti, while the peak at 531.6 eV is attributed to C=O or C–OH.[53] The peak at 532.8 eV is ascribed to Ti–O–C, and is an indication of the covalent interaction between TiO_2 and SWCNTs.[54] Based on density functional theory calculations,[55] Ti–O–C bonds facilitate charge carrier separation due to their higher electrostatic density in comparison to the non-covalent interaction. As a consequence, the charge redistribution map predicts a higher rate of electron transport. The C 1s region, shown in Fig. 3d, is

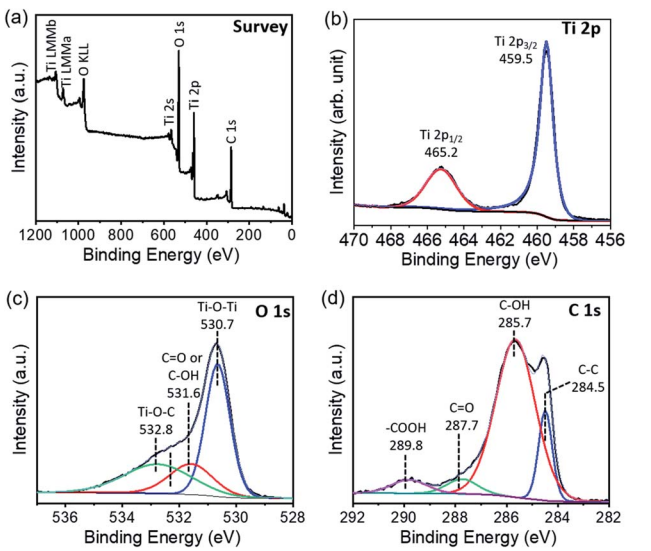

Fig. 3 XPS spectra of TiO_2-short SWCNT. (a) XPS survey spectrum; deconvolution of high-resolution Ti 2p spectrum (b), O 1s spectrum (c), and C 1s spectrum (d).

fitted with four peak components. The peak at 284.5 eV is assigned to sp^2 carbon, while the peaks at 285.7, 287.7, and 289.8 eV are assigned to functional groups linked to the carbon atoms including C–O/C–O–Ti, C=O, and O–C=O, respectively.[54,56] The various oxygen functional groups generate anchors for direct linking with TiO_2. The absence of the Ti–C peak, typically located at 281 eV,[57] confirms our claim regarding the absence of significant carbon doping in the composite.

3.2. Photocatalytic degradation of gaseous acetaldehyde by TiO_2–SWCNT hybrids

To evaluate the photocatalytic activity of TiO_2 wrapped with SWCNTs, the degradation of acetaldehyde was conducted under UV light. Fig. 4a shows the effect of SWCNT amount in the hybrid structure on photocatalytic activity expressed in terms of normalized acetaldehyde concentration after 60 minutes. Coupling of short SWCNTs with TiO_2 markedly improves degradation of acetaldehyde. The photocatalytic degradation activity is sensitive to the amount of SWCNTs in the composite; our findings revealed the optimum amount to be 1 wt%. A schematic illustration of the proposed mechanism for photocatalytic degradation of gaseous acetaldehyde on TiO_2-short SWCNT hybrid is depicted in Fig. 4b. Upon light illumination, photo-induced electron–hole pairs are produced by TiO_2 ($h\nu$ (<350 nm) $\rightarrow e^-_{CB+SWCNTs} + h^+$); the electrons are promoted to the conduction band leaving holes in the valance band.[58] The CB position of anatase is ~4.21 eV using vacuum level (AVS) (−0.4 eV relative to reversible hydrogen electrode (RHE)), with a bandgap of about 3.2 eV. On the other hand, the work function of a SWCNT is known to be ~−4.8 eV (AVS) (approximately 0.2 relative to RHE).[59] Since the work function of SWCNTs is lower than the conduction band of TiO_2, SWCNTs can act as electron sinks whereby a fraction of the photoelectrons flow to them.[41,59] The holes in the valence band react with water molecules to generate hydroxyl radicals ($^{\bullet}OH$) ($H_2O + h^+ \rightarrow {}^{\bullet}OH + H^+$), while the photoexcited electrons in SWCNTs and in the conduction band of TiO_2 react with O_2 to produce superoxide radicals ($^{\bullet}O_2^-$) ($O_2 + e^-_{CB+SWCNTs} \Rightarrow {}^{\bullet}O_2^-$). The active radicals initiate decomposition of adsorbed gaseous acetaldehyde *via* two reaction pathways. $^{\bullet}OH$ and $^{\bullet}O_2^-$ could oxidize a portion of acetaldehyde to carbon dioxide and water ($CH_3CHO \overset{{}^{\bullet}OH/{}^{\bullet}O_2^-}{\Rightarrow} CO_2 + H_2O$). The remaining acetaldehyde could be oxidized to acetic acid by $^{\bullet}OH$ in the first step ($CH_3CHO \overset{{}^{\bullet}OH}{\Rightarrow} CH_3COOH$) and subsequently converted to water and carbon dioxide by $^{\bullet}O_2^-$ in a second step ($CH_3CHO \overset{{}^{\bullet}O_2^-}{\Rightarrow} CO_2 + H_2O$).[58,60–62] As shown in Fig. 4c, the relevant potential level of the acceptor species is located below the CB potential of TiO_2. On the other hand, the potential level of the donor species is above the valence band position of TiO_2, validating the generation of active radicals responsible for the degradation of gaseous acetaldehyde.[63–69]

It is well known the photogenerated electron–hole pair participates in redox reactions on the catalyst surface to initiate degradation of adsorbed pollutant; however, the process is limited by rapid recombination of electrons and holes. As depicted in Fig. 4b, one of the roles of SWCNTs in TiO_2–CNT composites is to inhibit electron–hole recombination.[15,16] An increase in the amount of SWCNTs in the hybrid composite beyond 1 wt% has a negative effect on the photocatalytic performance, which we attribute to SWCNT aggregation and generation of large SWCNT bundles. Hsu and coworkers[70–75] have provided further mechanistic insight into the effect of nanocarbon loading on photocatalytic performance. The overall charge separation efficiency in nanocarbon-semiconductor hybrids can be sacrificed when the amount of the electron sink (metal or nanocarbon) exceeds the optimum value. The observed trend in activity for the different TiO_2–SWCNT ratios in our study is consistent with the results from these studies and can also be rationalized by the so called later-emerging electron–hole recombination that is induced across the interface. The formation of large-diameter bundles indicates SWCNTs at high concentration tend to interact with each other *via* Van der Waals forces rather than with TiO_2. As a consequence, the quality of the interfacial contact (or degree of interaction) between TiO_2 and SWCNTs is reduced. In addition, the coverage of thick SWCNT bundles on TiO_2 particles has the potential of significantly decreasing light penetration to TiO_2,

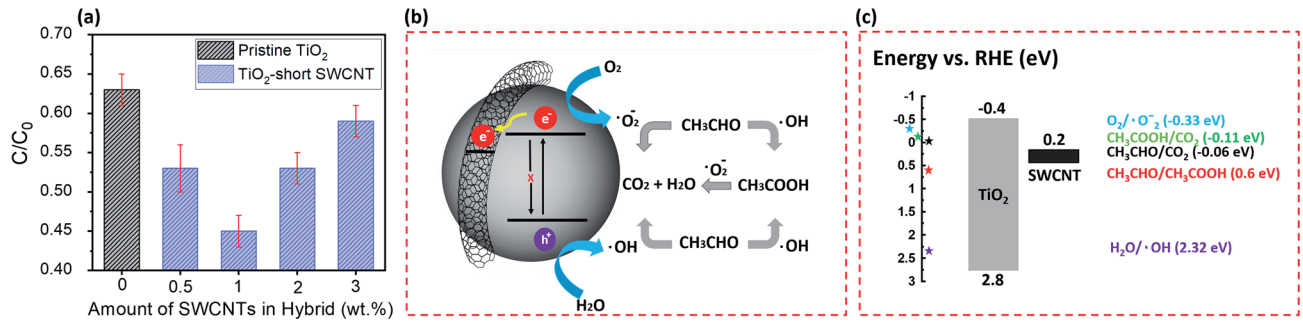

Fig. 4 (a) Photocatalytic degradation of gaseous acetaldehyde using TiO_2 and TiO_2-short SWCNT of different SWCNT loadings after 60 minutes. (b) Schematic illustration of the possible mechanism of photocatalytic degradation of gaseous acetaldehyde. (c) Band edge position of a TiO_2–SWCNT hybrid relative to reversible hydrogen electrode (RHE) with approximated values of redox potentials of active radicals/compounds involved in degradation of gaseous acetaldehyde.

thus reducing photoactivity as observed in other studies that involve wrapping of graphene on TiO_2 or coupling graphene quantum dots with TiO_2.[41,76] Despite the decrease in photocatalytic activity upon SWCNT aggregation, the observed performance is still higher than pristine TiO_2, indicating photon permeation is not completely blocked and the beneficial role of SWCNTs in photocatalytic enhancement, *via* charge separation, may still be partially maintained.

3.3. Effect of SWCNT length and graphitic dimensions on interfacial contact, charge separation, and photocatalytic activity of the hybrids

To probe the influence of SWCNT length on the interfacial contact and subsequent photocatalytic performance of TiO_2–SWCNT hybrids, we synthesized another composite with long SWCNTs (TiO_2-long SWCNT) using the same concentration of SWCNTs, but without subjecting the sample to the ultrasonication cutting step. Representative TEM images for long SWCNTs and short SWCNTs used for coupling with TiO_2 are presented in Fig. S5† with corresponding box plots in Fig. 5 showing their length distributions; each box plot consists of 12 measurements of nanotubes from TEM images. The average length of short SWCNTs is 125 ± 90 nm while that of long SWCNTs is 1.2 ± 0.67 μm. The results clearly demonstrate the shear force generated by ultrasonication results in SWCNTs that are significantly shorter than those processed without ultrasonication. The use of ultrasonication as a nondestructive technique for cutting nanotubes is well established in processing nanomaterials. Shuba *et al.*[77] showed that ultrasonication yields SWCNTs with low side-wall degradation and preserves the electronic properties of the nanotubes. Note that for SWCNTs to efficiently play the intended role of "electron sink" in hybrid structures during photocatalysis, preserving their structural integrity and exceptional electronic properties is critically important.

The Raman spectra of pristine SWCNTs, short SWCNTs, and long SWCNTs in Fig. 6 provide further insight into the effect of the processing approach on the structure of SWCNTs. The ratio of G- to D-band intensities (I_G/I_D) from the Raman spectra, widely considered a quality or graphitization index for carbon-based materials,[78–80] is 13.9 for pristine SWCNTs and decreases to 3.3 and 3.6 after acid treatment for long SWCNTs and short SWCNTs, respectively, due to the functionalization of SWCNTs. The I_G/I_D ratios for short and long SWCNTs are about the same, which indicates that the ultrasonication process did not degrade the nanotubes. As observed previously in Fig. 2b, the TiO_2–SWCNT composite exhibited a slight decrease in I_G/I_D, suggesting the increase in defect after the coupling of TiO_2 and SWCNTs,[49] probably due to the low substitution of Ti^{4+} by carbon atoms. In addition, the characteristic phonon mode in SWCNTs occurring in the low frequency region (zoomed in the insets), the radial breathing mode (RBM), is clearly observed in pristine and processed SWCNTs. In fact, the same RBM peaks for pristine SWCNTs at ~150 and 260 cm^{-1} are observed for long SWCNTs and short SWCNTs. This provides further evidence that the ultrasonication process did not destroy the nanotubes.

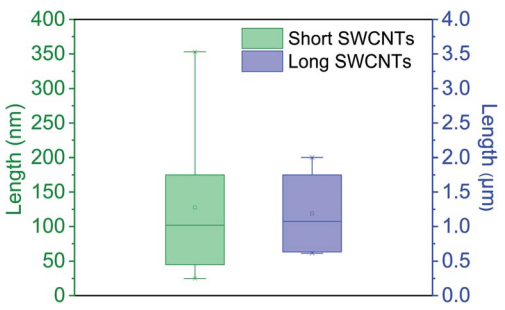

Fig. 5 Box plots showing lengths of short SWCNTs and long SWCNTs. Each box plot consists of 12 measurements of nanotubes from TEM images.

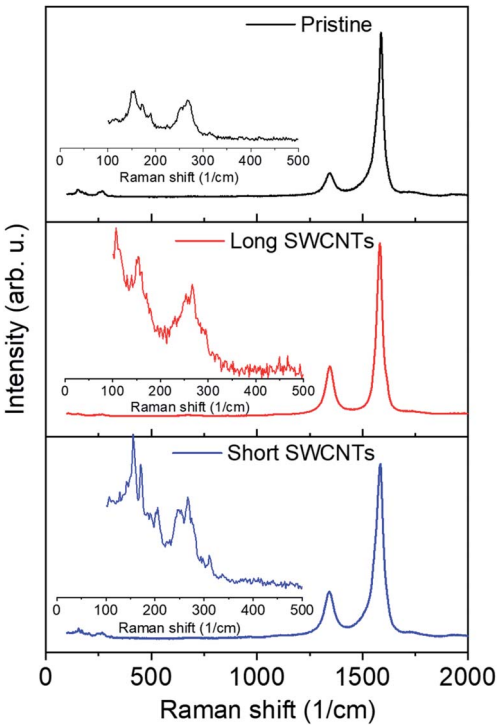

Fig. 6 Raman spectra of pristine SWCNTs, long SWCNTs and short SWCNTs with insets showing zoom-in spectra of RBMs in the lower frequency region.

Next, we investigate the effect of SWCNT length and nanocarbon dimension on interfacial contact, charge separation, and photocatalytic activity of the hybrids. Electron microscopic images of the resulting hybrids formed with short SWCNTs, long SWCNTs and nanographene, along with corresponding EDS mapping for TiO_2–nanographene, are shown in Fig. 7. The EDS mapping of TiO_2–nanographene reveal a highly uniform distribution of titanium, carbon, and oxygen as observed for TiO_2-short SWCNT (Fig. 1b). In contrast to TiO_2-short SWCNT (Fig. 7a), bundles of large-diameter SWCNTs are apparent in TiO_2-long SWCNT composites (Fig. 7b), with severe particle aggregation as shown in Fig. S6.† These observations give credence to the assumption that ultrasonication not only reduces the length of SWCNTs, but also facilitates debundling of SWCNTs. Morphological characterization of micron-sized

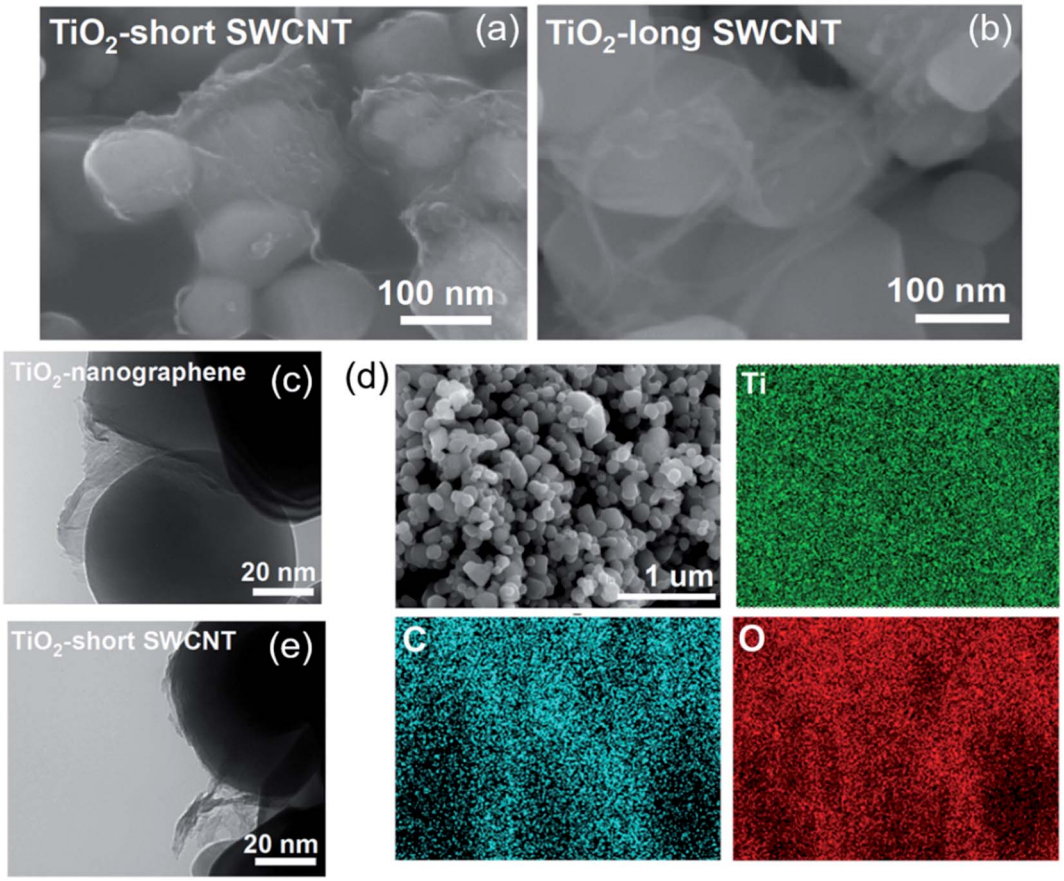

Fig. 7 SEM images of TiO_2-short SWCNT (a) and TiO_2-long SWCNT (b). TEM image of TiO_2–nanographene (c) and corresponding EDS mapping (d). TEM image of TiO_2-short SWCNT (e).

graphene, exfoliated nanographene, and non-exfoliated nanographene are summarized in Fig. S7.† The average size the nanographene, as determined from TEM analysis and shown on the box plot (Fig. S7†), is ~125 ± 93 nm.

Photocatalytic degradation of acetaldehyde by TiO_2, TiO_2-long SWCNT, TiO_2–nanographene, and TiO_2-short SWCNT, is shown in Fig. 8a along with the PL spectra of the photocatalysts in Fig. 8b. As depicted in Fig. 8a, TiO_2-short SWCNT shows the highest performance; the rate constant of TiO_2-short SWCNT is 0.015 min^{-1}, while others are given as follows: pristine TiO_2 (k = 0.0073 min^{-1}), TiO_2-long SWCNT (k = 0.0107 min^{-1}), and TiO_2–nanographene (k = 0.0125 min^{-1}). TiO_2-short SWCNT showed better performance compared with TiO_2–nanographene, even though the quality of interfacial contact in the two heterostructures is somewhat similar, as evidenced by EDS mapping that reveals a highly uniform distribution of nanographene on TiO_2 particles

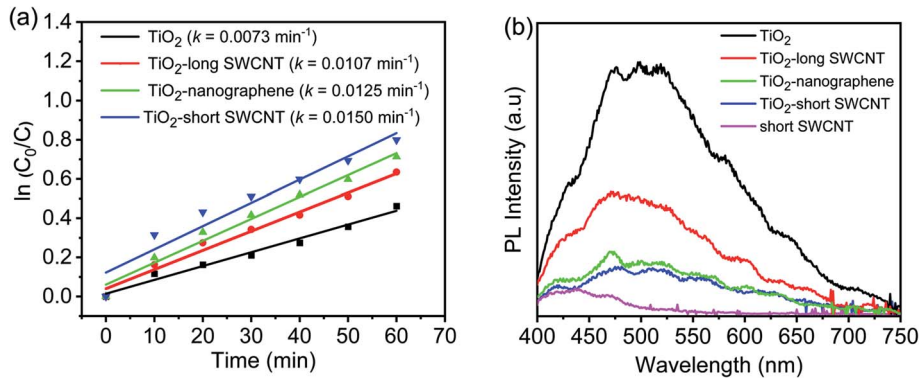

Fig. 8 (a) Photocatalytic activity of TiO_2, TiO_2-short SWCNT and TiO_2-long SWCNT during degradation of gaseous acetaldehyde based on a pseudo first-order kinetic model. (b) Photoluminescence (PL) spectra of TiO_2, TiO_2-long SWCNT, TiO_2–nanographene, TiO_2-short SWCNT, and short SWCNT.

over a large area (Fig. 7d). The PL spectra (Fig. 8b) show lifetimes of charges on TiO_2 coupled with short SWCNTs are longer than TiO_2 coupled with nanographene, which explains the different photocatalytic activities observed as evidenced by their rate constants.

4. Discussion

Based on our results, we present a schematic illustration of the interfacial contact between nanocarbon (short SWCNTs, long SWCNTs or nanographene) and TiO_2, as well as the charge carrier movement in the hybrids in Fig. 7. We rationalize the superior performance of TiO_2-short SWCNT to be due to the inhibition of charge recombination in the composite, which can be achieved in two ways. First, the increase in the number of interfacial contacts between each individual TiO_2 and short SWCNTs provides more channels for electron transport that inhibits charge recombination. The short and well-exfoliated SWCNTs can have lower bending stiffness compared to the long and non-exfoliated SWCNTs. It has been shown that bending stiffness of SWCNTs is directly proportional to SWCNT diameter;[81] therefore, we expect large-diameter SWCNT bundles to have larger persistence length compared to exfoliated SWCNTs (or small-diameter SWCNT bundles). Hence, short SWCNTs efficiently wrap a TiO_2 particle (Fig. 9a). Consequently, a large fraction of TiO_2 nanoparticles are in direct contact with short SWCNTs. In contrast, only a small fraction of TiO_2 nanoparticles are in direct contact with the long SWCNTs (Fig. 9b). Second, the improved SWCNT debundling ensures a uniform distribution of SWCNTs over a large area on the TiO_2 surface, and hence, the shuttling of electrons across the interface for enhanced charge separation is not restricted to a small portion of the composite as in the case of TiO_2-long SWCNT hybrids. To test the above hypotheses, PL data presented in Fig. 8b provide valuable insight. In comparison to pristine TiO_2, fluorescence quenching was observed in the TiO_2–SWCNT hybrid structures, confirming the transfer of electrons from TiO_2 to SWCNTs delayed charge recombination. It is clear from the PL results that the intensity of TiO_2-short SWCNT hybrids is lower than that of TiO_2-long SWCNT hybrids, and is substantially lower than pristine TiO_2, confirming the efficient charge separation occurring in TiO_2-short SWCNT hybrids.

To rationalize the role of short SWCNTs (or oxygen-containing functionalities), we have to consider the synthesis steps, and in particular, the zeta potentials of SWCNTs and TiO_2 particles in ethanol under the pH used. Factors such as type of solvent and pH of mixture can alter the surface charge of nanostructures. In our case, acid treatment lowers the zeta potential of SWCNTs due to the formation of oxygen functionalities as shown by Liu *et al.*[82] These functional groups on the surface and tips of short SWCNTs imparts a strong negative charge and make them more easily dispersed. The negatively charged groups provide a strong electrostatic attraction toward positively charged species. Conversely, at low pH or high hydrogen ion activity, the surface of TiO_2 acquires a positive charge due to the high zeta potential. In fact, Widegren and Bergström[83] showed that the addition of a relatively small amount of acid or base is capable of introducing a relatively strong charge on TiO_2 particles. In our synthesis experiment, TiO_2 particles and functionalized SWCNTs were dispersed in ethanol at pH = 3.5 which creates an environment with a high hydrogen activity and a strong positive charge on TiO_2. The strong positively charged TiO_2 particles and negatively charged functionalized SWCNTs interact strongly *via* electrostatic attraction to form the hybrid structures with enhanced interfacial contact. In addition, opened and unblocked CNTs significantly increase the density of adsorption or anchoring sites.[84] Cutting of long SWCNTs increases the number of open ends, and therefore, the short SWCNTs provide more "handles" or anchoring sites for interactions with TiO_2 than long SWCNTs.

The dimension of the graphitic structure is another important factor that can affect charge separation. To understand the role of the dimension of the graphitic structure in the composite, we compared the performance of TiO_2 quasi-wrapped by 1D SWCNTs (TiO_2-short SWCNT) with the quasi-wrapped by 2D nanographene (TiO_2–nanographene). The synthesis of the quasi-core–shell structure is adapted from a technique proposed by Kim *et al.*[36] We hypothesize that random pathways in 2D graphene can significantly reduce the

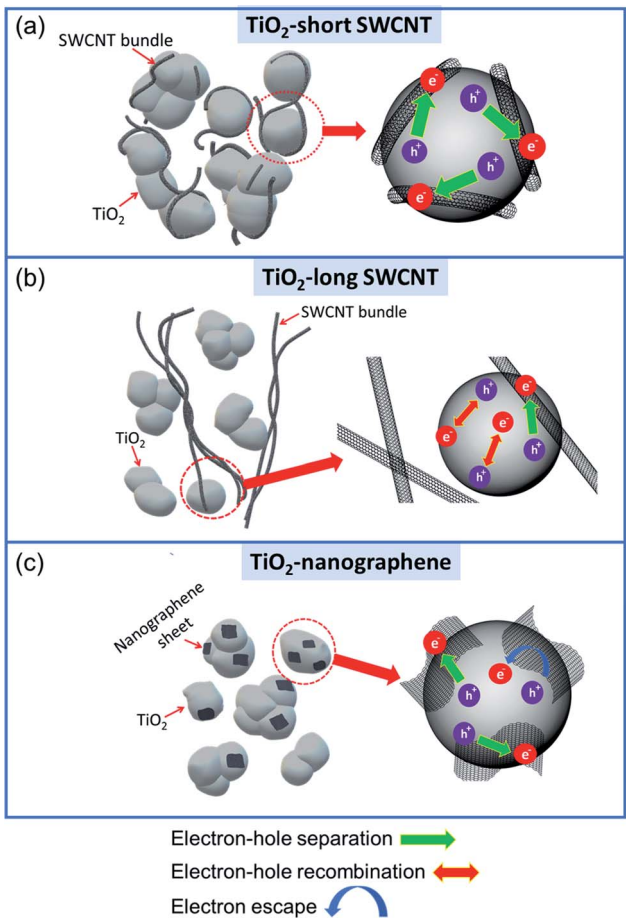

Fig. 9 Schematic illustrations of interfacial contact between nanocarbon and TiO_2, and charge carrier movement in TiO_2-short SWCNT (a), TiO_2-long SWCNT (b), and TiO_2–nanographene (c).

electron transport rate or may lead to electron escape from the graphene sheet (as schematically depicted in Fig. 9c), and thus promote charge carrier recombination. In contrast, the 1D SWCNTs offer efficient and short pathways for the transfer of vectorial electrons and, hence, enhanced charge separation. In addition, nanographene has a high stacking tendency and even after exfoliation, the number of layers cannot be easily controlled. During TEM analysis, we observed several TiO_2 nanoparticles with thick graphitic shells, considerably thicker than SWCNT bundles (see Fig. 7c and e). This means significant portion of incident light is hindered from reaching TiO_2 in a typical core–shell structure for TiO_2–nanographene. On the other hand, SWCNTs, even in the case of bundles, due to their one-dimensional structure and small diameters, do not completely block light permeation to TiO_2, as shown earlier for hybrid structures synthesized using high SWCNT concentrations. Nevertheless, coupling short SWCNTs or nanographene significantly improved electron–hole separation and photoreactivity of TiO_2; the photoexcited electrons in the TiO_2 core are efficiently transported into the nanocarbon due to the strong interfacial contact between the hybrid components.

5. Conclusions

TiO_2 nanoparticles quasi-wrapped with short SWCNTs were successfully fabricated *via* an approach that involves the interaction between TiO_2 and short SWCNTs in ethanol as a solvent. The presence of short SWCNTs resulted in enhanced photocatalytic activity and efficient charge separation. The improved interfacial contact, verified by electron microscopy, prolonged the lifetime of an electron–hole pair on TiO_2 as demonstrated by photoluminescence spectroscopy. Unlike hybrid structures with long SWCNTs, higher photocatalytic performance in gas-phase degradation of acetaldehyde was achieved with TiO_2-short SWCNT hybrids, confirming use of short SWCNTs in coupling with TiO_2 as a better alternative. Investigations into the effect of nanocarbon dimensions on charge separation revealed TiO_2-short SWCNT hybrids have slightly higher photocatalytic activity than TiO_2–nanographene. We attribute the performance to electron scattering in 2D-nanographene, which may affect electron transport through the interface. The high stacking tendency of nanographene may form a thick graphitic layer on TiO_2 that could hinder UV light penetration. Overall, this study provides rational new guidelines for maximizing electron–hole separation in TiO_2–nanocarbon hybrids for improved photocatalytic performance.

Conflicts of interest

There are no conflicts to declare.

Acknowledgements

This study was financially supported by the National Science Foundation (Grant No. 1653527).

References

1 S.-Y. Lee and S.-J. Park, TiO2 photocatalyst for water treatment applications, *J. Ind. Eng. Chem.*, 2013, **19**, 1761–1769.
2 A. Al Mayyahi, TiO_2 Polyamide Thin Film Nanocomposite Reverses Osmosis Membrane for Water Desalination, *Membranes*, 2018, **8**, 66.
3 Y. Sheng, Z. Wei, H. Miao, W. Yao, H. Li and Y. Zhu, Enhanced organic pollutant photodegradation *via* adsorption/photocatalysis synergy using a 3D g-C_3N_4/TiO_2 free-separation photocatalyst, *Chem. Eng. J.*, 2019, **370**, 287–294.
4 V. Puddu, H. Choi, D. D. Dionysiou and G. L. Puma, TiO_2 photocatalyst for indoor air remediation: Influence of crystallinity, crystal phase, and UV radiation intensity on trichloroethylene degradation, *Appl. Catal., B*, 2010, **94**, 211–218.
5 C. H. Ao and S. C. Lee, Indoor air purification by photocatalyst TiO_2 immobilized on an activated carbon filter installed in an air cleaner, *Chem. Eng. Sci.*, 2005, **60**, 103–109.
6 P. B. Amama, K. Itoh and M. Murabayashi, Gas-phase photocatalytic degradation of trichloroethylene on pretreated TiO_2, *Appl. Catal., B*, 2002, **37**, 321–330.
7 P. B. Amama, K. Itoh and M. Murabayashi, Effect of RuO_2 deposition on the activity of TiO_2: Photocatalytic oxidation of trichloroethylene in aqueous phase, *J. Mater. Sci.*, 2004, **39**, 4349–4351.
8 P. B. Amama, K. Itoh and M. Murabayashi, Photocatalytic oxidation of trichloroethylene in humidified atmosphere, *J. Mol. Catal. A: Chem.*, 2001, **176**, 165–172.
9 P. B. Amama, K. Itoh and M. Murabayashi, Photocatalytic degradation of trichloroethylene in dry and humid atmospheres: role of gas-phase reactions, *J. Mol. Catal. A: Chem.*, 2004, **217**, 109–115.
10 V. Rodríguez-González, S. Obregón, O. A. Patrón-Soberano, C. Terashima and A. Fujishima, An approach to the photocatalytic mechanism in the TiO_2-nanomaterials microorganism interface for the control of infectious processes, *Appl. Catal., B*, 2020, **270**, 118853.
11 P. Ganguly, C. Byrne, A. Breen and S. C. Pillai, Antimicrobial activity of photocatalysts: Fundamentals, mechanisms, kinetics and recent advances, *Appl. Catal., B*, 2018, **225**, 51–75.
12 E. I. Cedillo-González, R. Riccò, M. Montorsi, M. Montorsi, P. Falcaro and C. Siligardi, Self-cleaning glass prepared from a commercial TiO_2 nano-dispersion and its photocatalytic performance under common anthropogenic and atmospheric factors, *Build Environ.*, 2014, **71**, 7–14.
13 Q. Yi, H. Wang, S. Cong, Y. Cao, Y. Wang, Y. Sun, Y. Lou, J. Zhao, J. Wu and G. Zou, Self-Cleaning Glass of Photocatalytic Anatase TiO_2@Carbon Nanotubes Thin Film by Polymer-Assisted Approach, *Nanoscale Res. Lett.*, 2016, **11**, 457.
14 T. Zhu, Y. Cheng, J. Huang, J. Xiong, M. Ge, J. Mao, Z. Liu, X. Dong, Z. Chen and Y. Lai, A transparent

superhydrophobic coating with mechanochemical robustness for anti-icing, photocatalysis and self-cleaning, *Chem. Eng. J.*, 2020, **399**, 125746.

15 J. Schneider, M. Matsuoka, M. Takeuchi, J. Zhang, Y. Horiuchi, M. Anpo and D. W. Bahnemann, Understanding TiO_2 Photocatalysis: Mechanisms and Materials, *Chem. Rev.*, 2014, **114**, 9919–9986.

16 K. Lee, H. Yoon, C. Ahn, J. Park and S. Jeon, Strategies to improve the photocatalytic activity of TiO_2: 3D nanostructuring and heterostructuring with graphitic carbon nanomaterials, *Nanoscale*, 2019, **11**, 7025–7040.

17 X. Pan, Y. Zhao, S. Liu, C. L. Korzeniewski, S. Wang and Z. Fan, Comparing Graphene-TiO_2 Nanowire and Graphene-TiO_2 Nanoparticle Composite Photocatalysts, *ACS Appl. Mater. Interfaces*, 2012, **4**, 3944–3950.

18 W. Wang, P. Serp, P. Kalck and J. L. Faria, Visible light photodegradation of phenol on MWNT-TiO_2 composite catalysts prepared by a modified sol–gel method, *J. Mol. Catal. A: Chem.*, 2005, **235**, 194–199.

19 G. Lui, J.-Y. Liao, A. Duan, Z. Zhang, M. Fowler and A. Yu, Graphene-wrapped hierarchical TiO_2 nanoflower composites with enhanced photocatalytic performance, *J. Mater. Chem. A*, 2013, **1**, 12255–12262.

20 X. Hao, Z. Jin, J. Xu, S. Min and G. Lu, Functionalization of TiO_2 with graphene quantum dots for efficient photocatalytic hydrogen evolution, *Superlattices Microstruct.*, 2016, **94**, 237–244.

21 B. M. Everhart, M. Baker-Fales, B. McAuley, E. Banning, H. Almkhelfe, T. C. Back and P. B. Amama, Hydrothermal synthesis of carbon nanotube–titania composites for enhanced photocatalytic performance, *J. Mater. Res.*, 2020, **35**, 1451–1460.

22 K. Woan, G. Pyrgiotakis and W. Sigmund, Photocatalytic Carbon-Nanotube–TiO_2 Composites, *Adv. Mater.*, 2009, **21**, 2233–2239.

23 M. Shaban, A. M. Ashraf and M. R. Abukhadra, TiO_2 Nanoribbons/Carbon Nanotubes Composite with Enhanced Photocatalytic Activity; Fabrication, Characterization, and Application, *Sci. Rep.*, 2018, **8**, 781.

24 V. Štengl, D. Popelková and P. Vláčil, TiO_2–Graphene Nanocomposite as High Performance Photocatalysts, *J. Phys. Chem. C*, 2011, **115**, 25209–25218.

25 K. Zhou, Y. Zhu, X. Yang, X. Jiang and C. Li, Preparation of graphene–TiO_2 composites with enhanced photocatalytic activity, *New J. Chem.*, 2011, **35**, 353–359.

26 A. Miribangul, X. Ma, C. Zeng, H. Zou, Y. Wu, T. Fan and Z. Su, Synthesis of TiO_2/CNT Composites and its Photocatalytic Activity Toward Sudan (I) Degradation, *Photochem. Photobiol.*, 2016, **92**, 523–527.

27 Y. Yang, L. Xu, H. Wang, W. Wang and L. Zhang, TiO_2/graphene porous composite and its photocatalytic degradation of methylene blue, *Mater. Design*, 2016, **108**, 632–639.

28 Z. Li, B. Gao, G. Z. Chen, R. Mokaya, S. Sotiropoulos and G. Li Puma, Carbon nanotube/titanium dioxide (CNT/TiO_2) core–shell nanocomposites with tailored shell thickness, CNT content and photocatalytic/photoelectrocatalytic properties, *Appl. Catal., B*, 2011, **110**, 50–57.

29 J. Yu, T. Ma and S. Liu, Enhanced photocatalytic activity of mesoporous TiO_2 aggregates by embedding carbon nanotubes as electron-transfer channel, *Phys. Chem. Chem. Phys.*, 2011, **13**, 3491–3501.

30 W. Yao, Y. Li, D. Yan, M. Ma, Z. He, S. Chai, X. Su, F. Chen and Q. Fu, Fabrication and photocatalysis of TiO_2-graphene sandwich nanosheets with smooth surface and controlled thickness, *Chem. Eng. J.*, 2013, **229**, 569–576.

31 B. Gao, C. Peng, G. Z. Chen and G. Li Puma, Photo-electro-catalysis enhancement on carbon nanotubes/titanium dioxide (CNTs/TiO_2) composite prepared by a novel surfactant wrapping sol–gel method, *Appl. Catal., B*, 2008, **85**, 17–23.

32 X.-H. Xia, Z.-J. Jia, Y. Yu, Y. Liang, Z. Wang and L.-L. Ma, Preparation of multi-walled carbon nanotube supported TiO_2 and its photocatalytic activity in the reduction of CO2 with H2O, *Carbon*, 2007, **45**, 717–721.

33 W. Zhang, G. Li, H. Liu, J. Chen, S. Ma and T. An, Micro/nano-bubble assisted synthesis of Au/TiO_2@CNTs composite photocatalyst for photocatalytic degradation of gaseous styrene and its enhanced catalytic mechanism, *Environ. Sci.: Nano*, 2019, **6**, 948–958.

34 B. Gao, G. Z. Chen and G. Li Puma, Carbon nanotubes/titanium dioxide (CNTs/TiO_2) nanocomposites prepared by conventional and novel surfactant wrapping sol–gel methods exhibiting enhanced photocatalytic activity, *Appl. Catal., B*, 2009, **89**, 503–509.

35 C. Wang, D. Meng, J. Sun, J. Memon, Y. Huang and J. Geng, Graphene Wrapped TiO_2 Based Catalysts with Enhanced Photocatalytic Activity, *Adv. Mater. Interfaces*, 2014, **1**, 1300150.

36 H.-i. Kim, G.-h. Moon, D. Monllor-Satoca, Y. Park and W. Choi, Solar Photoconversion Using Graphene/TiO_2 Composites: Nanographene Shell on TiO_2 Core *versus* TiO_2 Nanoparticles on Graphene Sheet, *J. Phys. Chem. C*, 2012, **116**, 1535–1543.

37 Y. Dai, Y. Sun, J. Yao, D. Ling, Y. Wang, H. Long, X. Wang, B. Lin, T. H. Zeng and Y. Sun, Graphene-wrapped TiO_2 nanofibers with effective interfacial coupling as ultrafast electron transfer bridges in novel photoanodes, *J. Mater. Chem. A*, 2014, **2**, 1060–1067.

38 H. R. Jafry, M. V. Liga, Q. Li and A. R. Barron, Single walled carbon nanotubes (SWNTs) as templates for the growth of TiO_2: the effect of silicon in coverage and the positive and negative synergies for the photocatalytic degradation of Congo red dye, *New J. Chem.*, 2011, **35**, 400–406.

39 L. Ling, C. Wang, M. Ni and C. Shang, Enhanced photocatalytic activity of TiO_2/single-walled carbon nanotube (SWCNT) composites under UV-A irradiation, *Sep. Purif. Technol.*, 2016, **169**, 273–278.

40 K. Dai, X. Zhang, K. Fan, T. Peng and B. Wei, Hydrothermal synthesis of single-walled carbon nanotube–TiO_2 hybrid and its photocatalytic activity, *Appl. Surf. Sci.*, 2013, **270**, 238–244.

41 Y. Yao, G. Li, S. Ciston, R. M. Lueptow and K. A. Gray, Photoreactive TiO_2/Carbon Nanotube Composites:

Synthesis and Reactivity, *Environ. Sci. Technol.*, 2008, **42**, 4952–4957.

42 R. Seshadri, H. N. Aiyer, A. Govindaraj and C. N. R. Rao, Electron transport properties of carbon nanotubes, *Solid State Commun.*, 1994, **91**, 195–199.

43 W. S. Hummers and R. E. Offeman, Preparation of Graphitic Oxide, *J. Am. Chem. Soc.*, 1958, **80**, 1339.

44 W.-C. Hu, Y.-A. Chen, P.-Y. Hsieh, C.-W. Tsao, Y.-H. Chiu, T.-F. M. Chang, C.-Y. Chen, M. Sone and Y.-J. Hsu, Reduced graphene oxides-wrapped ZnO with notable photocatalytic property, *J. Taiwan Inst. Chem. Eng.*, 2020, **112**, 337–344.

45 K.-A. Tsai and Y.-J. Hsu, Graphene quantum dots mediated charge transfer of CdSe nanocrystals for enhancing photoelectrochemical hydrogen production, *Appl. Catal., B*, 2015, **164**, 271–278.

46 Y. Huang, D. Chen, X. Hu, Y. Qian and D. Li, Preparation of TiO_2/Carbon Nanotubes/Reduced Graphene Oxide Composites with Enhanced Photocatalytic Activity for the Degradation of Rhodamine B, *Nanomaterials*, 2018, **8**, 431.

47 Y. Li, Z. Wang and X.-J. Lv, N-doped TiO_2 nanotubes/N-doped graphene nanosheets composites as high performance anode materials in lithium-ion battery, *J. Mater. Chem. A*, 2014, **2**, 15473–15479.

48 F. Wang and K. Zhang, Physicochemical and photocatalytic activities of self-assembling TiO_2 nanoparticles on nanocarbons surface, *Curr. Appl. Phys.*, 2012, **12**, 346–352.

49 B. Chai, T. Peng, X. Zhang, J. Mao, K. Li and X. Zhang, Synthesis of C60-decorated SWCNTs (C60-d-CNTs) and its TiO2-based nanocomposite with enhanced photocatalytic activity for hydrogen production, *Dalton Trans.*, 2013, **42**, 3402–3409.

50 T. Appadurai, C. M. Subramaniyam, R. Kuppusamy, S. Karazhanov and B. Subramanian, Electrochemical Performance of Nitrogen-Doped TiO_2 Nanotubes as Electrode Material for Supercapacitor and Li-Ion Battery, *Molecules*, 2019, **24**, 2952.

51 W. Li, R. Liang, N. Y. Zhou and Z. Pan, Carbon Black-Doped Anatase TiO_2 Nanorods for Solar Light-Induced Photocatalytic Degradation of Methylene Blue, *ACS Omega*, 2020, **5**, 10042–10051.

52 R. Taziwa, E. L. Meyer and K. G. Chinyama, Raman temperature dependence analysis of carbon-doped titanium dioxide nanoparticles synthesized by ultrasonic spray pyrolysis technique, *J. Mater. Sci.*, 2012, **47**, 1531–1540.

53 G. An, W. Ma, Z. Sun, Z. Liu, B. Han, S. Miao, Z. Miao and K. Ding, Preparation of titania/carbon nanotube composites using supercritical ethanol and their photocatalytic activity for phenol degradation under visible light irradiation, *Carbon*, 2007, **45**, 1795–1801.

54 W. Vallejo, A. Rueda, C. Díaz-Uribe, C. Grande and P. Quintana, Photocatalytic activity of graphene oxide–TiO_2 thin films sensitized by natural dyes extracted from Bactris guineensis, *R. Soc. Open Sci.*, 2019, **6**, 181824.

55 S. Ayissi, P. A. Charpentier, K. Palotás, N. Farhangi, F. Schwarz and W. A. Hofer, Preferential Adsorption of TiO_2 Nanostructures on Functionalized Single-Walled Carbon Nanotubes: A DFT Study, *J. Phys. Chem. C*, 2015, **119**, 15085–15093.

56 Z. Hu, Y. Huang, S. Sun, W. Guan, Y. Yao, P. Tang and C. Li, Visible light driven photodynamic anticancer activity of graphene oxide/TiO_2 hybrid, *Carbon*, 2012, **50**, 994–1004.

57 H. Wu, J. Fan, E. Liu, X. Hu, Y. Ma, X. Fan, Y. Li and C. Tang, Facile hydrothermal synthesis of TiO_2 nanospindles-reduced graphene oxide composite with a enhanced photocatalytic activity, *J. Alloys Compd.*, 2015, **623**, 298–303.

58 Q. Zeng, X. Xie, X. Wang, Y. Wang, G. Lu, D. Y. H. Pui and J. Sun, Enhanced photocatalytic performance of Ag@TiO_2 for the gaseous acetaldehyde photodegradation under fluorescent lamp, *Chem. Eng. J.*, 2018, **341**, 83–92.

59 Y. Yao, G. Li, S. Ciston, R. M. Lueptow and K. A. Gray, Photoreactive TiO_2/Carbon Nanotube Composites: Synthesis and Reactivity, *Environ. Sci. Technol.*, 2008, **42**, 4952–4957.

60 H. Hu, W.-j. Xiao, J. Yuan, J.-w. Shi, M.-x. Chen and W.-f. Shang Guan, Preparations of TiO_2 film coated on foam nickel substrate by sol-gel processes and its photocatalytic activity for degradation of acetaldehyde, *J. Environ. Sci.*, 2007, **19**, 80–85.

61 X. Ye, D. Chen, J. Gossage and K. Li, Photocatalytic oxidation of aldehydes: Byproduct identification and reaction pathway, *J. Photochem. Photobiol., A*, 2006, **183**, 35–40.

62 A. H. Mamaghani, F. Haghighat and C.-S. Lee, Photocatalytic oxidation technology for indoor environment air purification: The state-of-the-art, *Appl. Catal., B*, 2017, **203**, 247–269.

63 H. Huang, B. Pradhan, J. Hofkens, M. B. J. Roeffaers and J. A. Steele, Solar-Driven Metal Halide Perovskite Photocatalysis: Design, Stability, and Performance, *ACS Energy Lett.*, 2020, **5**, 1107–1123.

64 X. Zhao, L. Du, B. You and Y. Sun, Integrated design for electrocatalytic carbon dioxide reduction, *Catal. Sci. Technol.*, 2020, **10**, 2711–2720.

65 R. D. Feinman, Oxidation-reduction calculations in the biochemistry course, *Biochem. Mol. Biol. Educ.*, 2004, **32**, 161–166.

66 W. He, H.-K. Kim, W. G. Wamer, D. Melka, J. H. Callahan and J.-J. Yin, Photogenerated Charge Carriers and Reactive Oxygen Species in ZnO/Au Hybrid Nanostructures with Enhanced Photocatalytic and Antibacterial Activity, *J. Am. Chem. Soc.*, 2014, **136**, 750–757.

67 A. L. Linsebigler, G. Lu and J. T. Yates, Photocatalysis on TiO_2 Surfaces: Principles, Mechanisms, and Selected Results, *Chem. Rev.*, 1995, **95**, 735–758.

68 M.-J. Fang, C.-W. Tsao and Y.-J. Hsu, Semiconductor nanoheterostructures for photoconversion applications, *J. Phys. D: Appl. Phys.*, 2020, **53**, 143001.

69 Y.-H. Chiu, T.-F. M. Chang, C.-Y. Chen, M. Sone and Y.-J. Hsu, Mechanistic Insights into Photodegradation of Organic Dyes Using Heterostructure Photocatalysts, *Catalysts*, 2019, **9**, 430.

70 Y.-C. Chen, K.-i. Katsumata, Y.-H. Chiu, K. Okada, N. Matsushita and Y.-J. Hsu, ZnO–graphene composites as practical photocatalysts for gaseous acetaldehyde

degradation and electrolytic water oxidation, *Appl. Catal., A*, 2015, **490**, 1–9.

71 Y.-C. Chen, Y.-C. Pu and Y.-J. Hsu, Interfacial Charge Carrier Dynamics of the Three-Component In_2O_3–TiO_2–Pt Heterojunction System, *J. Phys. Chem. C*, 2012, **116**, 2967–2975.

72 Y.-H. Hsu, A. T. Nguyen, Y.-H. Chiu, J.-M. Li and Y.-J. Hsu, Au-decorated GaOOH nanorods enhanced the performance of direct methanol fuel cells under light illumination, *Appl. Catal., B*, 2016, **185**, 133–140.

73 W.-H. Lin, Y.-H. Chiu, P.-W. Shao and Y.-J. Hsu, Metal-Particle-Decorated ZnO Nanocrystals: Photocatalysis and Charge Dynamics, *ACS Appl. Mater. Interfaces*, 2016, **8**, 32754–32763.

74 Y.-F. Lin and Y.-J. Hsu, Interfacial charge carrier dynamics of type-II semiconductor nanoheterostructures, *Appl. Catal., B*, 2013, **130–131**, 93–98.

75 Y.-C. Pu, H.-Y. Chou, W.-S. Kuo, K.-H. Wei and Y.-J. Hsu, Interfacial charge carrier dynamics of cuprous oxide-reduced graphene oxide (Cu2O-rGO) nanoheterostructures and their related visible-light-driven photocatalysis, *Appl. Catal., B*, 2017, **204**, 21–32.

76 D. Pan, J. Jiao, Z. Li, Y. Guo, C. Feng, Y. Liu, L. Wang and M. Wu, Efficient Separation of Electron–Hole Pairs in Graphene Quantum Dots by TiO_2 Heterojunctions for Dye Degradation, *ACS Sustainable Chem. Eng.*, 2015, **3**, 2405–2413.

77 M. V. Shuba, A. G. Paddubskaya, P. P. Kuzhir, S. A. Maksimenko, V. K. Ksenevich, G. Niaura, D. Seliuta, I. Kasalynas and G. Valusis, Soft cutting of single-wall carbon nanotubes by low temperature ultrasonication in a mixture of sulfuric and nitric acids, *Nanotechnology*, 2012, **23**, 495714.

78 L. Bokobza, J.-L. Bruneel and M. Couzi, Raman Spectra of Carbon-Based Materials (from Graphite to Carbon Black) and of Some Silicone Composites, *Carbon*, 2015, **1**, 77–94.

79 S. Santangelo, Controlled surface functionalization of carbon nanotubes by nitric acid vapors generated from sub-azeotropic solution, *Surf. Interface Anal.*, 2016, **48**, 17–25.

80 P. B. Amama, C. Lan, B. A. Cola, X. Xu, R. G. Reifenberger and T. S. Fisher, Electrical and Thermal Interface Conductance of Carbon Nanotubes Grown under Direct Current Bias Voltage, *J. Phys. Chem. C*, 2008, **112**, 19727–19733.

81 N. Fakhri, D. A. Tsyboulski, L. Cognet, R. B. Weisman and M. Pasquali, Diameter-dependent bending dynamics of single-walled carbon nanotubes in liquids, *Proc. Natl. Acad. Sci.*, 2009, **106**, 14219.

82 Y. Liu, L. Gao, J. Sun and Y. Wang, Functionalization of carbon nanotubes for nanoparticle attachment, *J. Ceram. Process. Res.*, 2010, **11**, 120–122.

83 J. Widegren and L. Bergström, Electrostatic Stabilization of Ultrafine Titania in Ethanol, *J. Am. Ceram. Soc.*, 2004, **85**, 523–528.

84 X. Ren, C. Chen, M. Nagatsu and X. Wang, Carbon nanotubes as adsorbents in environmental pollution management: A review, *Chem. Eng. J.*, 2011, **170**, 395–410.